DOI: 10.1002/ejic.200601176

Assembly and Formation of Biomorphic Tin Dioxide by a Biomimetic Sol–Gel Approach Involving Glycoprotein

Qun Dong,[a] Huilan Su,*[a] Wei Cao,[a] Di Zhang,[a] Qixin Guo,[b] and Fangying Zhang[c]

Keywords: Biomimetic synthesis / Colloids / Hierarchy / Nanotubes / Sol–gel processes

Three diverse layers of eggshell membrane (ESM) were introduced in a biogenic sol–gel technique for the synthesis of hierarchical SnO_2 nanomaterials with corresponding configurations. Typically, the biomorphic replication of the interwoven inner eggshell membrane was systematically investigated by controlling synthesis conditions such as pH value, dipping time, and calcination temperature. The as-prepared SnO_2 tubes consisting of interconnected 5-nm nanocrystallite units were successfully interwoven into ESM-morphic films. Herein, the biomaterial ESM served both as the physical substrate and the functional macromolecule template to realize the precision replication, by the interactions between ESM macromolecules (containing carboxyl, hydroxy, amino groups, etc.) and Sn colloid ingredients. Moreover, some biomacromolecules also acted as the surfactant to yield small-scaled and well-distributed SnO_2 nanocrystallites based on the strong bondage of short-chained amino acids within ESM glycoprotein with SnO_2 nuclei. This technique can be attributed to a biomimetic sol–gel process and is widely applicable to the synthesis of other functional material systems.

Introduction

Lately, nanoscale functional materials have attracted much attention because of their potentially excellent and fascinating properties. In the progressive stage, the assembly of the nanoscale units into a hierarchical architecture would be required to obtain higher functionality and performance. Nevertheless, there are few feasible reports on the construction of hierarchical nanomaterials, especially practical and functional metal or metal oxide nanocomposites. Notably, natural organisms or biological structures that have evolved as a result of highly complex and elegant mechanisms[1] are a great inspiration for materials scientists and chemists in the imitation of the hierarchical structures. The work in this field is based on the premise that amphiphilic and bioorganic macromolecules could be utilized for tailoring elaborate structures through the self-assembly of nanoscale units[2] to engender new functional properties.[3] Quite a few biological species have been utilized to construct hierarchical inorganic materials: the list includes DNA,[4] viruses,[5] diatoms and skeletal plates,[6] butterfly wings,[7] shell membrane,[8] silk fiber,[9] hair,[10] wood,[11] and other plants (leaves, paper, pollen grains),[7,12] etc.

Recently, mimicking vital functions in aqueous systems has been noteworthy as a promising nanofabrication technique for functional materials.[3a,13] These biomimetic techniques enable the construction of hierarchical architectures including macro- and nanostructures by growing inorganic crystals with coexisting biospecies under ambient conditions. Quoting from Cook et al.,[7] "the synthetic replication of evidently useful biological structures by a simple casting process is expected to introduce some of the superb properties of biological structures into man-made materials." The most feasible method of attaining this goal at a high level seems to be the aqueous sol–gel technique.[14] The colloid components could interact with some biomacromolecules and undergo surface-preferred gelation to form the coats on the biomaterials, even to veraciously replicate the biotemplate frameworks down to the nanoscale. Moreover, the sol–gel process offers several advantages over other methods, including simplicity of procedure, lower processing temperature, and better homogeneity. Commonly, metallic alkoxides are used as starting materials to prepare fine-scaled metallic oxides by the sol–gel processes. However, metallic alkoxides are both expensive and extremely sensitive to moisture, heat, and light, implying that the process is relatively difficult to control and not economical. Therefore, various metal salts[15] are preferred as the precursors. Once biomaterials are introduced to the reformative sol–gel techniques, a series of intricate hydrolysis and condensation reactions happen in the sol–gel process. It seems to be a process that would enable the easy preparation of hierarchical

[a] State Key Lab of Metal Matrix Composites, Shanghai Jiaotong University,
Shanghai 200030, P. R. China
[b] Department of Electrical and Electronic Engineering, Saga University,
Saga 840-8502, Japan
[c] National Key Lab of Surface Physics, Fudan University,
Shanghai 200433, P. R. China
Fax: +86-21-62822012
E-mail: hlsu@sjtu.edu.cn
Supporting information for this article is available on the WWW under http://www.eurjic.org or from the author.

metal oxides, such as TiO_2, SiO_2, ZnO, ZrO_2, and so on. Therefore, biomimetic synthesis associated with the sol–gel technique would be an ideal approach for the design and fabrication of functional materials with predetermined physical and chemical properties.

Having a large bandgap of 3.6 eV at 300 K, a high achievable carrier concentration of up to 6×10^{20} cm^{-3}, and an expected exciton Bohr radius of about 2.4 nm,[16] nanocrystalline tin oxide is of great technological and scientific interest as a key functional semiconductor that is used extensively for photovoltaic devices,[17] transparent conductive electrodes,[18] gas sensors,[19] antistatic coatings,[20] dye-sensitized solar cells,[21] etc. It has also been demonstrated that, when such ultrafine nanocrystallites are arrayed into a macroscale hierarchical structure (such as tubes, hollow spheres, etc), these materials sometimes exhibit novel properties.[22] However, fresh tin gel has a hydrous skeleton and is either amorphous or pseudocrystalline. To achieve well-crystallized SnO_2, further calcination treatment at a higher temperature would be advisable to remove organic substrates and improve the stability and the purity of the target materials. As the growth of particles is controlled by the motion of the boundaries between the particles, calcination usually results in the increase and wider distribution of particle size.[23] Therefore, the growth inhibition of SnO_2 nanocrystallites was recently implemented with the addition of heterogeneous particles or in-situ secondary-phase particle generation. However, this solution may result in interface poisoning or poor purity. It has been discovered that, in biological systems such as diatoms and sponges, the formation of solid silica nanostructures with precisely controlled morphologies is the function of proteins and polysaccharides.[24] These biomacromolecules could direct and bind the nucleation and the growth of inorganic particles. Attracted by this bioinspiration, we introduce a convenient biomaterial, the eggshell membrane (ESM), in combination with a tin salt precursor, with the intent of synthesizing hierarchical SnO_2 semiconductors by suitable vehicles of special protein structures and functional residues of ESM biomacromolecules in a sol–gel process. In contrast to the metallic alkoxide precursors used by Yang et al.,[8] we attempted to employ a trilayer bio-scaffold in tin nitrate solution as a template for the structure of SnO_2. The natural trilayer ESM composed of the outer shell membrane (OSM), the inner shell membrane (ISM), and the limiting membrane (LM) with dissimilar hierarchical structures and morphologies, has been faithfully reproduced from the macroscopic to the nanometer scale by SnO_2 nanosemiconductors. Additionally, the reaction mechanism involving a biomimetic sol–gel process was explored. This method provides a simple but efficient and universal route to the biomimetic synthesis of advanced functional materials.

Results and Discussion

Overview of ESM Hierarchical Structures

The avian eggshell is composed of multilayered membranes and a calcified extracellular matrix, which are sequentially assembled during the motion of the egg along the oviduct.[25] The examination of cross-fractured eggshell by FESEM, shown in Figure 1a, reveals that the calcified shell is composed of an inner mammillary layer (ML) and an outer palisade layer (PL) resting upon the shell membranes. In fact, ESM consists of the organic OSM, ISM, and LM, which are nonmineralized, collagen-based matrices interposed between the egg white and the mineralized shell. From the images of ESM shown in Figure 1b, the three layers are readily distinguished. Sparsely deposited on the outer layer of the shell membranes are the mammillary knobs for penetrating into the tips of the mammillary cones. In addition, the interwoven and coalescing nature of the shell membrane fibers with an average width ranging from 500 nm to 2 μm is evident both in the OSM and the ISM. Furthermore, some of the broader fibers have a longitudinally striated appearance, where two or more narrower fibers join each other for part of their length. The amorphous LM shows an undulant appearance, which is due to a layer of spherical protein granules formed between the ISM and the LM. In this work, the distinct membranes were utilized as biotemplates for the synthesis of hierarchical SnO_2.

Characterization of Biomorphic Tin Dioxide

The calcination process was traced by conducting TGA and DTA surveys to follow the formation of hierarchical

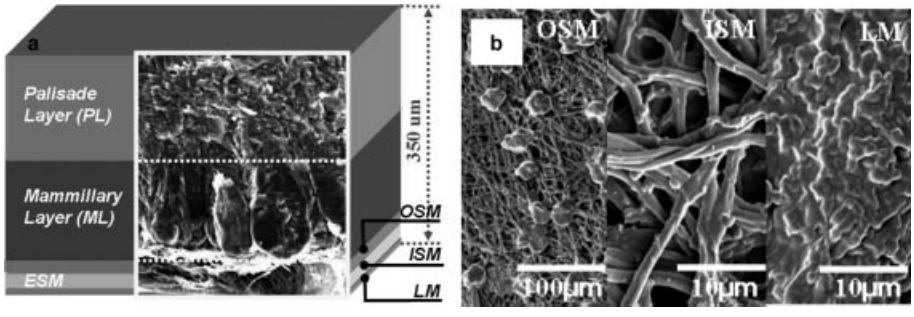

Figure 1. (a) FESEM images of eggshell and eggshell membrane and the corresponding schematic illustration of eggshell structures. (b) FESEM images of OSM, ISM, and LM.

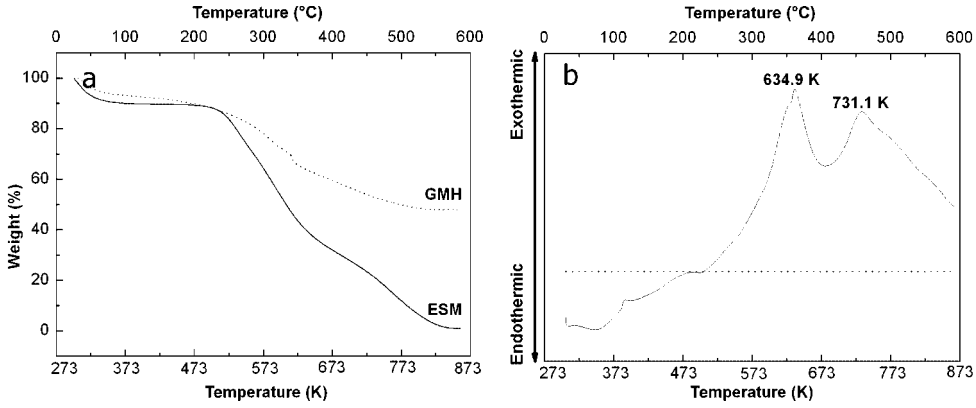

Figure 2. (a) TGA curves of the natural ESM and the intergradation of GMH; (b) DTA curve of GMH.

SnO_2. The corresponding curves for the natural ESM and gel–membrane hybrids (GMH) are shown in Figure 2. It is evident that the ESM starts pyrolyzing at 473 K and is absolutely decomposed by 823 K. Although GMH are also decomposed around 473 K, they can preserve up to 47.2% (by mass) inorganic matter at 823 K, at which temperature the organic ESM is completely removed. As seen from the differential curve, when GMH are heated from room temperature to 473 K, the weight loss of 9.8 wt-% is due to the removal of adsorbed water, and above 473 K they experience a two-step weight loss. Congruously, the DTA curve shows two peaks at 635 K and 731 K, which should represent the decomposition of Sn–ligand hybrids and organic ESM components, respectively.

To clarify the crystalline structure, the XRD patterns of the ESM and GMH as well as the corresponding sinters at 673 K and 823 K are shown in Figure 3. It can be seen that the natural ESM and GMH are totally amorphous. After calcination at 673 K, the amorphous hybrids are found to be crystallized. However, according to the TGA and DTA results, the ESM is not thoroughly decomposed at this temperature: although the intensities of some peaks are enhanced, there are new diffraction peaks accompanying the complete pyrolysis of ESM, indicating the well-established crystallization process at 823 K. All these diffraction peaks can be indexed to tetragonal SnO_2 with a rutile structure (JCPDS 41–1445), which indicates that the specimens consist of pure single tetragonal SnO_2. The fairly broadened diffraction peaks are assigned to SnO_2 nanocrystallites with very small dimensions. The average crystallite sizes of about 2.8 nm at 673 K and 5.2 nm at 823 K, are estimated according to the line-width analysis of the diffraction peaks based on the Scherrer formula. The chemical states of tin and oxygen during the sol–gel process were investigated by XPS analysis (Supporting Information, Figure S1). The corrected XPS spectra of the O1s emissions are different, where the peak with binding energy around 532.3 eV corresponds to the hydroxyl bonds of GMH, while the weaker peak around 531.1 eV corresponds to the Sn–O–Sn bonds of the sinters.[26] Moreover, GMH appear as a spin-orbit doublet at 487.9 ($3d_{5/2}$) and 496.4 eV ($3d_{3/2}$) in the Sn3d emission spectra with an area ratio of 1.5:1. Thus, the chemical state of the element tin in as-prepared GMH corresponds to Sn^{IV}, but not to Sn^{II} or Sn^{III}.

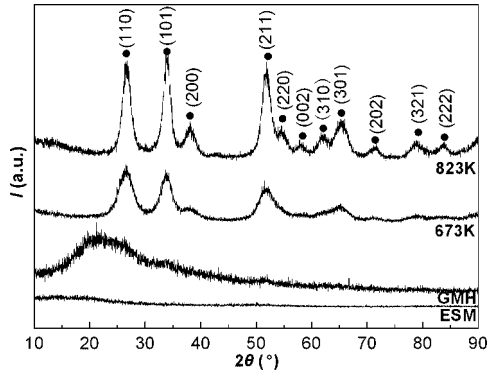

Figure 3. XRD patterns of the sinters calcined at 673 K and 823 K, compared with those of ESM and GMH.

It has been demonstrated that the interfacial sol–gel process is a facile chemical method to deposit ultrathin metal oxide layers with molecular precision.[27] This process is usually based on the chemical adsorption of metal alkoxides or metallic salts from the colloid medium onto the substrate surface to form a covalently bound monolayer, followed by hydrolysis to give a new hydroxylated gel layer for the successive film deposition. Organic molecules of the substrate can be readily incorporated as second components if they are reactive toward the as-deposited amorphous gel layer, thus the configuration and structure of the substrate can be accurately traced by the metal oxide network.[28] Here, the three diverse layers of organic ESM have the same ingredients containing amine, amide, and carboxyl surface functional groups, which may lead to complicated reactions to achieve the duplication of ESM configuration during the interfacial sol–gel process.

Representative FESEM images of as-prepared SnO_2 with various morphologies calcined at 823 K are shown in Figure 4a, 4b, and 4c. A comparison with the original OSM, ISM, and LM (insets) suggests that the refined reprography of the natural ESM hierarchy is achieved, although there

exists modest shrinkage. Analysis with energy-dispersive X-ray spectroscopy reveals that the atomic ratio Sn/O is close to 1:2, further confirming the stoichiometry of the replicas as SnO_2, in agreement with XRD results. As shown in Figure 4a, the obtained SnO_2 is composed of interwoven fibers and sparse crunodes depositing on the ceramic fibers with an average interval of about 18 μm. The interval is smaller than the original spacing of 30 μm as a result of heat shrinkage. Moreover, the refined meshworks of the natural OSM are also duplicated in addition to the larger intersectional crunodes. Figure 4b shows the interwoven and coalescing SnO_2 fibers ranging from 200 to 500 nm in diameter in comparison with the original ISM fibers. When using LM as the template, a lumpy layer of SnO_2 composed of consecutive ravines is obtained (Figure 4c). These special silkworm-like structures may come into being and array according to the spherical protein granules under the ultrathin LM. Therefore, it can be concluded that hierarchical SnO_2 accurately replicates the hierarchy of the biotemplate ESM from the OSM to the innermost LM. However, a shrinkage rate of nearly 55% is sometimes observed during the calcination treatment. By repeating the immersing manipulation, heat constringency in size could be lowed to below 30%, and up to 47.2% of the mass of the sinters was preserved without changes in configuration and structure.

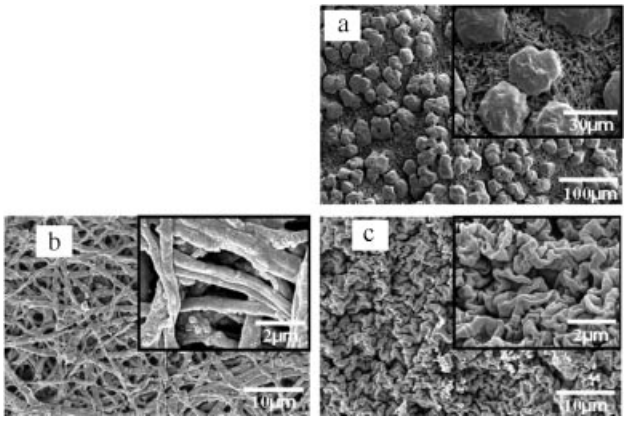

Figure 4. FESEM images of (a) OSM-based, (b) ISM-based, and (c) LM-based SnO_2. Insets show the corresponding detailed morphologies of the original OSM, ISM, and LM.

Figure 5a and 5b show the relative location of the hierarchical SnO_2 replicated from the three diverse membranes. It is clearly seen in Figure 5a that the LM-based one has been sheltered by the upper layers composed of the ISM-based and OSM-based SnO_2 layers. However, the replica of the LM layer can be identified when the other side of this sheet is observed (Figure 5b). The configuration of the intermeshed ISM consisting of interwoven fibers is intact, whereas the LM-based layer (denoted by an arrow) is curled up thoroughly. Moreover, the thickness of the obtained SnO_2 film can be tuned by removing the multilayers of the ISM. Thus, an SnO_2 film with a continuous thickness up to 20 μm can be achieved by varying the original thickness of remnant ISM layers (see Supporting Information, Figure S2). Figure 5c and 5d display higher magnifications of the cross section and the vertical section of these SnO_2 interwoven fibrous films, respectively. The tubular structures have an inner-diameter range from 100 nm to 300 nm and an average wall thickness of less than 90 nm. These SnO_2 tubes are rather uniform, and the hollow cores are glabrous and continuous throughout their length. Notably, these interwoven tubular structures are actually interconnected at junctions. A special kind of tube wrapping several smaller collateral cannulations is also observed, which likewise reproduces the original structures of the membrane fibers (see Supporting Information, Figure S3). To further investigate the replication process, we selected the organic ISM as a typical template to achieve the synthesis of hierarchical biomorphic SnO_2 under different experimental conditions.

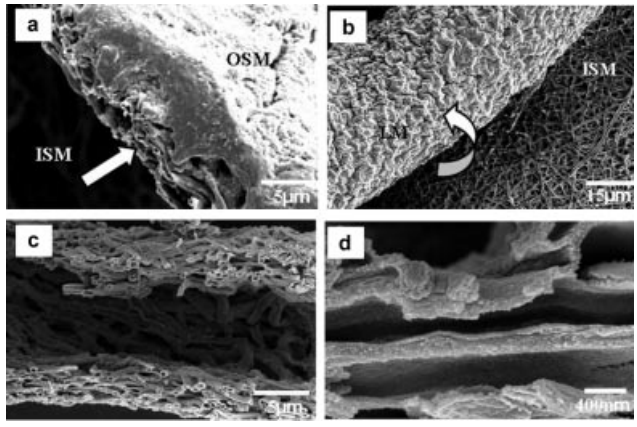

Figure 5. (a), (b) Typical FESEM images of as-prepared ISM-morphic SnO_2 revealing relative locations of the three distinct layers of the original ESM. (c), (d) FESEM images showing the cross-section and the vertical section of the ISM-based SnO_2, respectively.

Controllable Synthesis of ISM-Morphic SnO_2 Tubes

Figure 6 shows the micrographs of SnO_2 tubes synthesized at different calcination temperatures (823 to 1073 K). All the replicas have similar microscopic features and preserve the interwoven tubular structures of the natural ISM, but their building blocks, SnO_2 nanocrystallites, may grow with the increase in calcination temperature. The surface of SnO_2 tubes synthesized below 973 K looks more glazed in virtue of the smaller particle units, which was further proved by TEM results. Above 1073 K, the tubular structure is apparently composed of a network of interconnected SnO_2 particles, and it may collapse down into zonary form at 1273 K. On the contrary, if the calcination temperature is lowered to 673 K, characteristic tubular structures appear partially, and some look puffy, which may be caused by the organic remnants (see Supporting Information, Figure S4). It is reasonable that some residues of organic ESM remain at 673 K even though SnO_2 nanocrystallites have formed, which is in agreement with the TGA and XRD results.

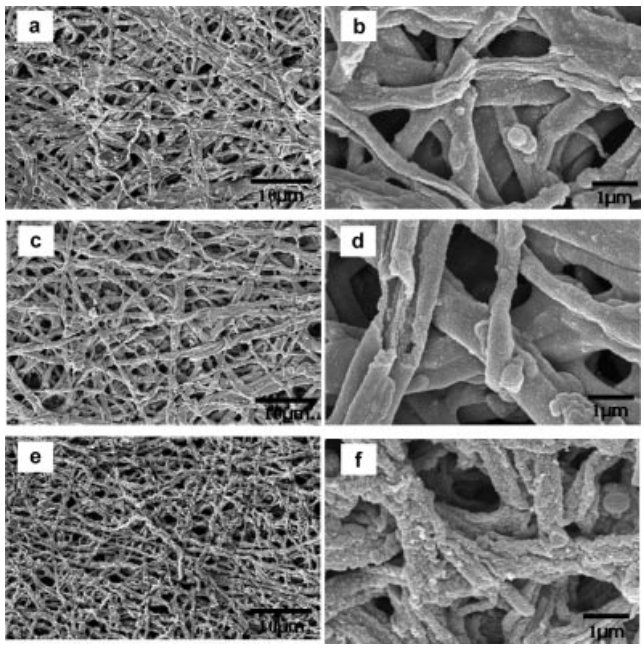

Figure 6. FESEM images of as-prepared ISM-morphic SnO_2 at different temperatures: (a) 823 K, (c) 973 K, and (e) 1073 K. Images (b), (d), and (f) show relevant higher magnifications of (a), (c), and (e), respectively.

Figure 7 gives the XRD patterns of the samples calcined at various temperatures between 823 and 1273 K for 1.5 h. All the diffraction peaks are assigned to the tetragonal rutile structure of SnO_2. It is found that the XRD peaks gradually become sharper with increasing temperature, indicating that the SnO_2 nanocrystallites grow larger. The crystallite sizes determined from the Scherrer equation are 5.2, 9.5, 10.3, and 20 nm, which have also been supported by the TEM results.

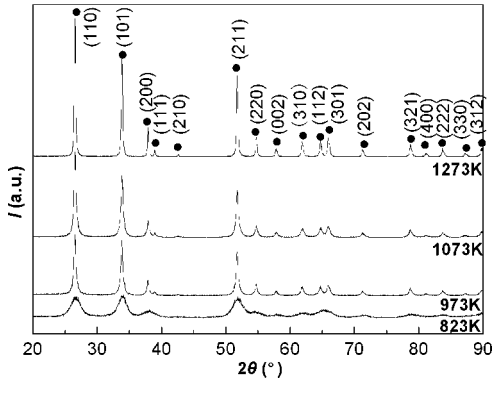

Figure 7. XRD patterns of ISM-based SnO_2 calcined at 823, 973, 1073, and 1273 K.

The TEM images in Figure 8a further reveal the tubular interwoven character of ISM-based SnO_2. The hollow tubular structure is clearly identified, and the wall thickness (50–60 nm) is found to be uniform along its entire length. This indicates that at 1073 K each tube has been transformed from a dense structure with a smooth surface into a highly porous structure consisting of interconnected nanocrystallites of ca. 10 nm in size (bottom inset in Figure 8a). In addition, the SAED patterns (top inset in Figure 8a) show that nanoscaled SnO_2 at 1073 K has polycrystalline tetragonal rutile structure (cassiterite) due to the uniform central and diffraction spots, and the diffraction rings are indexed to the (110), (101), (200), (211), and (301) diffractions of rutile-phase SnO_2. There are other supporting TEM data (see Supporting Information, Figure S5) supporting the construction of SnO_2 nanotubes by nanocrystallites calcined at different temperatures. Although the sinters at 673 K contain some impurities from ESM residues, the characteristic crystalline structure of tetragonal SnO_2 is observed in the electron diffraction image. This can be explained by the exothermic reactions occurring during the removal of the ESM: oxidation of the organic biomaterial emits heat locally, causing an increase in the temperature around the adsorbed Sn colloids, thereby accelerating the gelation and bringing on nanocrystalline SnO_2. These nanoparticles are ultrafine below 823 K while growing more quickly above 1073 K, and the average sizes of the nanoparticles are coincident with the crystallite sizes calculated from the XRD analyses by the Scherrer equation. As the nanoparticles grow with the increase in calcination temperatures, the diffraction patterns gradually transform from ring (nanoscale) to spot (bulk scale). This indicates that accurately defined, size-controlled SnO_2 nanoparticles in the range 2 to 20 nm are obtained to enable the construction of hierarchical nanomaterials at the corresponding calcination temperatures.

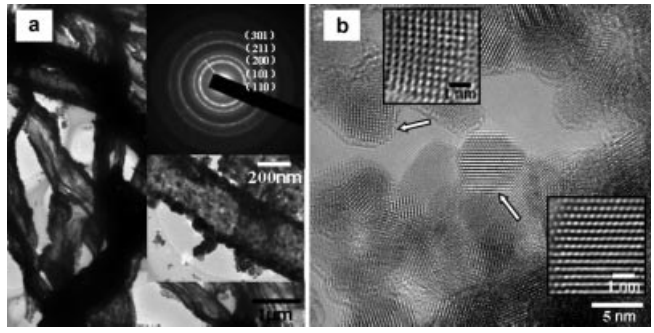

Figure 8. (a) TEM images of ISM-based SnO_2 synthesized at 1073 K and pH 1. Insets in (a) show an individual SnO_2 tube and the corresponding SAED pattern. (b) HRTEM image of ISM-based SnO_2 obtained at 823 K and pH 1. Insets in (b) correspond to the tetragonal SnO_2 (101) plane (top left) and the (110) plane (bottom right).

Figure 8b shows the typical HRTEM images of SnO_2 nanocrystallite units calcined at 823 K for 1.5 h. The lattice image can be clearly seen as a result of phase contrast. The distances between the adjacent lattice fringes correspond to the interplanar distances of the tetragonal SnO_2 (101) and (110), d_{101} = 0.264 nm and d_{110} = 0.335 nm, respectively. Considering that each domain having parallel lattice fringes is a single crystal of SnO_2, the average crystallite size is

observed to be 5 nm. The HRTEM results are in accord with the XRD analysis. A careful look at the images also reveals that the present SnO_2 is characterized by larger "nanostructured" particles consisting of nanocrystalline domains with structural defects such as twins.

Mechanism of the Biomimetic Sol–Gel Approach

To understand the multilevel interactions between the Sn colloids and the ESM biomacromolecules during the biomimetic sol–gel process, FTIR spectroscopic analysis was carried out on the original ESM, the GMH and the sinters. Figure 9 presents the typical FTIR spectra of GMH before and after calcination at 823 K compared with those of the original ISM. The spectrum of the original ISM shows the diagnostic peaks at 1641, 1532, and 1234 cm^{-1}, which are assigned to the amide I, amide II, and amide III bands of the proteins from the natural ISM, respectively. After interaction with the sol precursor, the red shift to 1630 cm^{-1} of the peak in the spectrum of GMH may be partly attributed to the superposition of the bending mode of water with the broad band around 3450 cm^{-1} (not 3400 cm^{-1}). The peak at 3430 to 3450 cm^{-1} is believed to be caused by adsorbed water. In general, the absorption band centered at 1630 cm^{-1}, as well as the one at 3450 cm^{-1}, is also ascribed to water adsorbed on the surface of the samples. Here, there would be no other corresponding peaks of amide I after immersion in the sol medium, if the peak at 1630 cm^{-1} (near 1620 cm^{-1}) in the spectrum of GMH were only due to the bending mode of water. The spectrum shows an increase in intensity of the amide I band relative to that of the amide II band. It does confirm the presence of a water deformation mode. Actually, the red shift of the amide I peak is probably overlapped by the above-mentioned water bending-mode peak. This red shift indicates that the C=O bonds in the peptide chains may be weakened because of the formation of new chelate bonds between C=O bonds and Sn colloids. This can be further corroborated by the NMR spectroscopic results (Supporting Information, Figure S6). It is also detected that the peak corresponds to the Sn–OH vibration band at around 3400 cm^{-1},[29] which is superimposed on the underlying C–H stretching signals of the polypeptides at 3290 cm^{-1} and close to the hydroxy bands of the water. As mentioned above, the bands of the sinters observed at around 3450 and 1630 cm^{-1} are assigned to the hydroxy bands of the adsorbed water. Below 700 cm^{-1}, the intense bands appearing both in GMH and the sinters at lower frequencies around 600 cm^{-1} are typical of the Sn–O–Sn antisymmetric and symmetric vibrations.[30] In addition, the bands appearing in the range between 850 and 1350 cm^{-1} are assigned to the bending mode of different types of surface hydroxy groups, which goes well with the previous research results.[31] The surface of the GMH could be terminated with the–OH groups after the ESM was dipped in the Sn sol medium. However, the calcination treatment would bring on weak IR bands between 850 and 1350 cm^{-1}, contributed by the decomposition of Sn–OH hydrate compounds into tin oxides. Accordingly, the interactions between Sn colloids and ESM macromolecules are mostly ascribed to the coordination of carboxyl, hydroxy, and other groups.

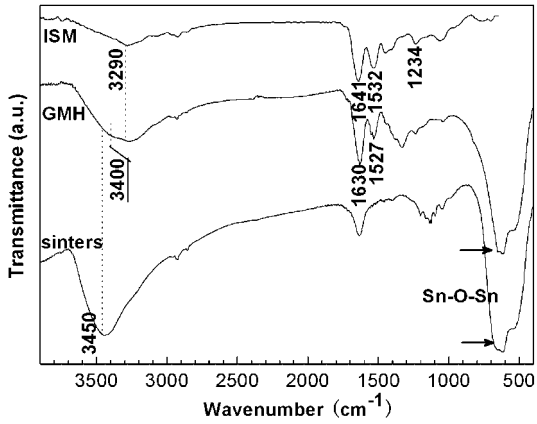

Figure 9. FTIR spectra of the original ISM, the corresponding GMH, and the relevant sinters at 823 K.

As we know, the shell membranes are nonmineralized, collagen-based matrices consisting of type I, V, and X collagens located in the core of each fiber. Each fiber is composed of a collagenous core surrounded by a glycoprotein mantle. It has been documented that the core is predominantly composed of collagen and osteopontin proteins, while the mantle is rich in polyanions exhibiting a variety of keratan sulfate (KS) epitopes and dermatan sulfate (DS).[25,32] Lysozyme and clusterin are also present at high levels in ESMs, and both have been detected within the membrane fibers, distributed discontinuously with no apparent partitioning between the core and the mantle. It is considered that the cationic lysozyme is bound to the anionic sites of DS and particularly those of KS in the membrane.[32b] Elegant studies[33] with clusterin have demonstrated that it exerts a powerful chaperone-like activity on lysozyme, as well as other purified proteins. Herein, the interfacial sol–gel process is presumably based on the adsorption of cationic groups from the colloid medium into the glycoprotein mantle of the ESM fiber containing an abundance of carboxylic, hydroxy, and amino residues; subsequently a series of complicated reactions proceed to give hierarchical SnO_2 films composed of ultrafine nanoparticles. The formation of SnO_2 can be denoted as follows:

$$Sn^0 \rightarrow Sn^{IV}\ \text{ions (hydrate ions)} \rightarrow Sn^{IV}\ \text{colloids} \rightarrow Sn^{IV}\text{oxo species (Sn–gel)} \rightarrow \text{amorphous } SnO_2 \rightarrow \text{nanocrystalline } SnO_2$$

The cationic Sn^{IV} species in the sol system are prone to interaction with the residues of the ESM glycoprotein, as proved by FTIR- and NMR spectroscopic results (Supporting Information, Figure S6). The formation of amorphous Sn colloid/glycoprotein hybrids arises from the strong binding affinity of some residues that involves multiple hydrogen bonds, van der Waals interactions, and the ordering of surface polypeptide loops. The Sn colloids are bound to the

amino groups of the glycoprotein in the biotemplate ESM and to the –OH and $–NH_2$ groups of the sugar chains linked to polypeptides. Amorphous Sn–O networks can be derived from these reactions, and indeed an amorphous SnO_2 film located in the mantle is obtained without changing the original morphologies at room temperature. The Sn^{IV} oxo species are assumed to be intermediates consisting of partly dehydrated polymeric Sn^{IV} hydroxides.

Amorphous SnO_2 ripens into well-defined nanocrystallites during the calcination treatment. Heat treatment frequently causes agglomeration and enlargement. However, SnO_2 nanocrystallites in our work have small size and good crystallization as well as a narrow size distribution (Supporting Information, Figure S7). This can probably be ascribed to some short-chained amino acids of glycoprotein, which function as capping agents, since the binding is strong enough for controlling the growth of tin dioxide nuclei.[34] For comparison, a blank sample is synthesized through a similar sol–gel approach and calcination treatment at 823 K only without using the biomaterials. SnO_2 nanoparticles in the blank sample are disorganized and have an average size of 21 nm, while the ESM-based SnO_2 nanocrystallites with an average size of 5 nm are arranged into orderly hierarchical structures. This observation proves the significance of the biotemplate and supports the above analysis. It is also concluded that the ESM peptidoglycan functioning as the surfactant may play a key role in the aggregation and further crystallization of tin oxide nanoparticles. In addition, electrostatic forces assist the biomimetic sol–gel process. Because of the higher acidity of the system (with ample H^+ ions), the tin oxide clusters in the colloid are likely to be positively charged at the surface by reference to the isoelectric point of cassiterite SnO_2 (7.3).[26] By electrostatic force, they would preferably attach onto the negatively charged $DS^–$ ions on the surface of the membrane. As surface coating is always dependent on surfactant concentration, it is difficult and complicated to determine the precise dosage. However, in our work the "surfactant molecules" could be released systematically by the dissociation and reforming of ESM biomolecules. With the aid of "surfactant molecules", the construction of biostructure hierarchy can be achieved to synthesize subtle biomorphic functional nanomaterials, which is similar to biomolecule-micelle systems.

Notably, a completely morphologic conversion from SnO_2 tubes to SnO_2 belts occurred as a result of tuning the pH value of the sol media. As lysozyme is a kind of protein that is unstable in alkaline medium, it is clear that the mantle of ESM fiber containing lysozyme is prone to dissociation, its glucide contents not in the collagenous core end up in the colloid system. Therefore, the resultant morphologies of the SnO_2 products might have an inherent affiliation with the structures and constituents of the glycoprotein mantle. It is observed that the mantle can exist as a steady covering layer at $pH < 2$, while the distortions and dissociations of this protein layer occur as the pH value is elevated. The mantle protein seems to flow and reform evidently when $pH > 3$, as depicted in Supporting Information (Figure S8). Under these circumstances, lysozyme is most active, and it functions as a kind of enzyme leading to the dissociation and disintegration of the peptidoglycan-based mantle layer. These protein chains then interact with the Sn colloids. Simultaneously, the proteins formerly carrying tubular hybrids start to dissociate and stretch into planar fibers as a result of decreased acidity as illustrated in Scheme 1. Moreover, it is revealed that clusterin, exhibiting powerful chaperone-like action on lysozyme, binds to and stabilizes aggregating proteins, thus leading to irreversible precipitation by preferentially recognizing partially folded protein conformations.[33] This process conduces to the stabilization of the final structures of SnO_2. The special layer thus makes it possible for SnO_2 fibers to transform from tubular to solid fibrous structures. However, the interaction of the strongly cationic lysozyme with the collagenous matrix may

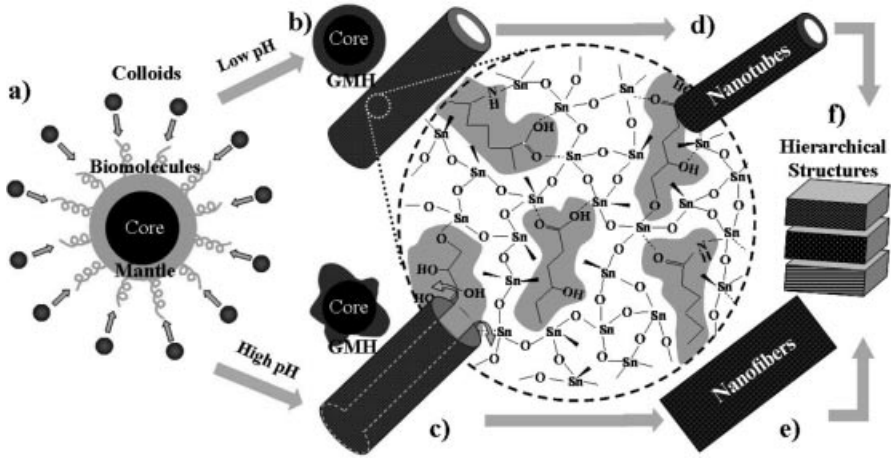

Scheme 1. Schematic depiction of hierarchical SnO_2 synthesized through the ESM-directed interfacial sol–gel process: (a) the cross-fractured ESM fiber showing its biomolecules interacting with Sn colloids; (b), (c) the stages of the mantle being immersed in the Sn sol media at different pH; the inset in (b) illustrates the interaction between the sol ingredients and the functional residues of ESM macromolecules after the removal of the ESM, (d) tubular SnO_2 and (e) SnO_2 fibrous belts; (f) hierarchical SnO_2 achieved by nanotube or nanobelt arrays.

be mediated by proteoglycans.[35] It is difficult for Sn colloids to interact with the core matrix under the current concentrations. Accordingly, hollow tubes form under higher acidity, while fibrous structures are obtained at lower acidity after the ESM is removed.

Prompted by their porous appearance and small-scale nanocrystalline units, we speculate that as-prepared hierarchical ESM-based SnO_2 must be useful in fabricating semiconducting sensors. When the grain size is reduced to a scale comparable to the space-charge length (for SnO_2, this value is 6 nm), the sensitivity could be exponentially enhanced.[23c,36] As an n-type semiconductor, SnO_2 has been extensively exploited in applications related to gas sensing. Most of these studies have focused on polycrystalline films made of small SnO_2 particles.[37] In contrast to some sensors made of individual single crystalline nanostructures or polycrystalline films, hierarchical nanostructured SnO_2 in our work, assembled by the small-scale, well-crystallized nanocrystallite units into tubular or zonary SnO_2 fibers with porous conformations and interconnected fibrous meshworks, would allow the sensors to be operated in the most sensitive, grain-controlled mode.

Conclusions

Hierarchical biomorphic SnO_2 has been successfully synthesized, by utilizing the biomaterial ESM as template, through a biomimetic sol–gel approach. The detailed configurations of three ESM layers from the outermost OSM to the ISM, then to the innermost LM, are duplicated with their typical mammillary knobs, interwoven fibers, and silkworm-like structures, respectively. Notably, the average size of SnO_2 nanocrystallite units could be tuned in the range 2 to 20 nm by the control over synthesis temperatures and could be restricted to an average size about 5 nm even at 823 K. It has been revealed that some functional groups such as the carboxyl, hydroxy, and amido groups of ESM macromolecules and the specific colloid medium as well as the relationship between them predominantly determine the formation of biomorphic SnO_2. ESM provides both a physical substrate and an inductive template for the interfacial sol–gel process to direct the chemical reactions between the sol ingredients and functional residues of ESM macromolecules. Moreover, on the basis of the "surfactant" action of short-chain amino acids of the ESM glycoprotein, the precision assembly from the nanoscale to the micrometer scale could be further realized. As-prepared hierarchical nanostructured films consisting of interwoven tubular SnO_2 with inner interconnectivity may be valuable gas-sensing materials in view of their intrinsically small grain size and high surface-to-volume ratios, allowing them to be operated in the most sensitive, grain-controlled mode. As a mild, green, and universal technique, biomimetic sol–gel synthesis is a versatile and feasible route to functional inorganic hierarchical materials. We envisage that, inspired by natural biostructures, the design and assembly of inorganic materials with predetermined structures and properties would lead to a new family of advanced functional systems.

Experimental Section

Preparation of the Biotemplates

Commercial eggs were gently broken and cleaned up. The eggshells were washed with distilled water, then the LM and the ISM were manually and successively removed. After the remaining eggshell was immersed in HCl solution (0.5 M) for 5 min, the OSM was separated from the $CaCO_3$ shell. All three layers of fresh membranes were washed with distilled water and subsequently dried by blast at room temperature. They were finally conserved in a vacuum desiccator for the following synthesis.

Synthesis of SnO_2 Hierarchical Nanomaterials

In a typical procedure, Sn powder (ca. 1.45 g) was added stepwise into HNO_3 solution (50 mL, 2 M) and stirred for 2 h. Then, distilled water (30 mL) was added slowly within 10 min to promote the hydrolysis of tin ions. It could be observed that a clear solution was obtained incipiently. It then turned into a slightly yellow colloid after being filtered. The pH values of the colloid media were generally kept at 1. For comparison, NaOH solution (1 M) was also added to modify the pH value of the media to 2 and 3. Then the OSM, the ISM, and the LM were immersed in the above-mentioned colloid systems for 13 h at room temperature. The GMH obtained were rinsed with distilled water and directly dried under air flow. Finally, the dry GMH were subjected to calcination treatments in air at 673 K, 823 K, 973 K, 1073 K, and 1273 K for 1.5 h. In all cases, white sheets were obtained and stored in vacuo for characterization.

Characterization

The morphology and composition were investigated with an FEI Sirion 200 field emission gun scanning electron microscope (FESEM) attached to an X-ray microanalyzer. Transmission electron microscopy (TEM) and high-resolution transmission electron microscopy (HRTEM) images were obtained as bright-field images and were examined by selected area electron diffraction (SAED), conducted with a JEOL JEM-2010 instrument and a JEOL JEM-2100F instrument, respectively. X-ray diffraction (XRD) measurements of the samples were carried out with a Rigaku Dmax 2550V instrument operating at a voltage of 40 kV and a current of 200 mA with Cu-K_α radiation (λ = 1.5406 Å) in the range 10–90°. X-ray photoelectron spectroscopy (XPS) was carried out with a VG Microlab 310F using Mg radiation to analyze the chemical states of tin oxide before and after calcination. Thermogravimetric analysis (TGA) and differential thermal analysis (DTA) were conducted to trace the calcination process with a TA 2050 thermoanalyzer and a TA 1600 thermal analysis system, respectively. For Fourier-transform infrared (FTIR) spectroscopy measurements, the spectra of the samples were recorded with a Bruker EQUINOX55 instrument at a resolution of 0.5 cm^{-1} and in a spectral range 4000–400 cm^{-1}.

Supporting Information (see footnote on the first page of this article): (1) XPS spectra of GMH and the sinters, (2) FESEM image of the biomorphic SnO_2 hierarchy, (3) FESEM images of tubular SnO_2 compared with the natural membrane fibers, (4) FESEM images of the interwoven ISM-based SnO_2 synthesized at 673 K and 1273 K, (5) TEM images of templated SnO_2 nanocrystallites synthesized at various temperatures, (6) MAS solid-state NMR spectra of original ESM and GMH, (7) TEM images of ISM-based SnO_2 nanocrystallites compared with the corresponding as-synthesized SnO_2 nanoparticles without template introduced through the same process, (8) FESEM images of GMH prepared at different pH values, (9) FESEM images of as-prepared intersectant SnO_2 fibers, and (10) nitrogen adsorption-desorption isotherms and

pore-size-distribution plots of ISM-templated SnO_2 and samples prepared without the biotemplate.

Acknowledgments

Financial support from NSFC (no. 50371055) and Shanghai Science and Technology Committee (nos. 04DZ14002, 0352nm051, 05nm05020) are gratefully acknowledged.

[1] a) S. A. Wainwright, *Mechanical Design in Organisms*, John Wiley & Sons, New York, **1976**; b) H. A. Lowenstam, *On Biomineralization*, Oxford University Press, Oxford, **1989**; c) S. Kamat, X. Su, R. Ballarini, A. H. Heuer, *Nature* **2000**, *405*, 1036–1040; d) M. Rubner, *Nature* **2003**, *423*, 925–926.
[2] a) H. Colfen, S. Mann, *Angew. Chem. Int. Ed.* **2003**, *42*, 2350–2365; b) M. Antonietti, G. A. Ozin, *Chem. Eur. J.* **2004**, *10*, 29–41.
[3] a) S. Mann, *Biomimetic Materials Chemistry*, VCH, Weinheim, **1996**; b) P. Vukusic, J. R. Sambles, *Nature* **2003**, *424*, 852–855; c) A. Sellinger, P. M. Weiss, A. Nguyen, Y. F. Lu, R. A. Assink, W. L. Gong, C. J. Brinker, *Nature* **1998**, *394*, 256–260.
[4] R. C. Mucic, J. J. Storhoff, C. A. Mirkin, R. L. Letsinger, *J. Am. Chem. Soc.* **1998**, *120*, 12674–12675.
[5] S. W. Lee, C. B. Mao, C. E. Flynn, A. M. Belcher, *Science* **2002**, *296*, 892–895.
[6] M. R. Weatherspoon, S. M. Allan, E. Hunt, Y. Cai, K. H. Sandhage, *Chem. Commun.* **2005**, 651–653.
[7] G. Cook, P. L. Timms, C. G. Spickermann, *Angew. Chem. Int. Ed.* **2003**, *42*, 557–559.
[8] a) D. Yang, L. M. Qi, J. M. Ma, *Adv. Mater.* **2002**, *14*, 1543–1546; b) D. Yang, L. M. Qi, J. M. Ma, *J. Mater. Chem.* **2003**, *13*, 1119–1123; c) D. Y. Zhang, L. M. Qi, *Chem. Commun.* **2005**, 2735–2737.
[9] Q. Dong, H. L. Su, D. Zhang, *J. Phys. Chem. B* **2005**, *109*, 17429–17434.
[10] Y. Kim, *Biomacromolecules* **2003**, *4*, 908–913.
[11] C. R. Rambo, H. Sieber, *Adv. Mater.* **2005**, *17*, 1088–1091.
[12] J. G. Huang, T. Kunitake, *J. Am. Chem. Soc.* **2003**, *125*, 11834–11835.
[13] a) S. Mann, *Biomineralization: Principles and Concepts in Bioinorganic Materials Chemistry*, Oxford University Press, New York, **2001**; b) R. A. Caruso, *Angew. Chem. Int. Ed.* **2004**, *43*, 2746–2748.
[14] R. A. Caruso, M. Antonietti, *Chem. Mater.* **2001**, *13*, 3272–3282.
[15] a) N. Shirahata, W. Shin, N. Murayama, A. Hozumi, Y. Yokogawa, T. Kameyama, Y. Masuda, K. Koumoto, *Adv. Funct. Mater.* **2004**, *14*, 580–588; b) B. Cheng, J. M. Russell, W. S. Shi, L. Zhang, E. T. Samulski, *J. Am. Chem. Soc.* **2004**, *126*, 5972–5973; c) G. S. Pang, S. G. Chen, Y. Koltypin, A. Zaban, S. H. Feng, A. Gedanken, *Nano Lett.* **2001**, *1*, 723–726.
[16] S. Ferrere, A. Zaban, B. A. Gregg, *J. Phys. Chem. B* **1997**, *101*, 4490–4493.
[17] D. A. Gaal, J. T. Hupp, *J. Am. Chem. Soc.* **2000**, *122*, 10956–10963.
[18] D. S. Ginley, C. Bright, *Mater. Res. Soc. Bull.* **2000**, *25*, 15–18.
[19] a) G. J. Li, X. H. Zhang, S. Kawi, *Sens. Actuators B* **1999**, *60*, 64–70; b) A. Kolmakov, Y. X. Zhang, G. S. Cheng, M. Moskovits, *Adv. Mater.* **2003**, *15*, 997–1000.
[20] H. Ogawa, A. Abe, M. Nishikawa, S. Hayakawa, *J. Electrochem. Soc.* **1981**, *128*, 2020–2025.
[21] Z. W. Pan, Z. R. Dai, Z. L. Wang, *Science* **2001**, *291*, 1947–1949.
[22] Y. L. Wang, X. C. Jiang, Y. N. Xia, *J. Am. Chem. Soc.* **2003**, *125*, 16176–16177.
[23] a) Y. M. Chiang, *Physical Ceramics: Principles for Ceramic Science and Engineering*, John Wiley & Sons, New York, **1997**; b) C. J. Brinker, *Sol–Gel Science: The Physics and Chemistry of Sol–Gel Processing*, Academic Press, San Diego, **1990**; c) N. L. Wu, S. Y. Wang, I. A. Rusakova, *Science* **1999**, *285*, 1375–1377.
[24] J. N. Cha, G. D. Stucky, D. E. Morse, T. J. Deming, *Nature* **2000**, *403*, 289–292.
[25] M. S. Fernandez, M. Araya, J. L. Arias, *Matrix Biol.* **1997**, *16*, 13–20.
[26] C. H. Liang, Y. Shimizu, T. Sasaki, N. Koshizaki, *J. Phys. Chem. B* **2003**, *107*, 9220–9225.
[27] a) I. Ichinose, H. Senzu, T. Kunitake, *Chem. Mater.* **1997**, *9*, 1296–1298; b) W. Jones, *Supramolecular Organization and Materials Design*, Cambridge University Press, Cambridge, **2002**.
[28] a) I. Ichinose, T. Kawakami, T. Kunitake, *Adv. Mater.* **1998**, *10*, 535–539; b) T. Kunitake, S. W. Lee, *Anal. Chim. Acta* **2004**, *504*, 1–6.
[29] P. Salas, J. G. Hernandez, J. A. Montoya, J. Navarrete, J. Salmones, I. Schifter, J. Morales, *J. Mol. Catal. A: Chem.* **1997**, *123*, 149–154.
[30] V. M. Jimenez, A. Caballero, A. Fernandez, J. P. Espinos, M. Ocana, A. R. Gonzalez-Elipe, *Solid State Ionics* **1999**, *116*, 117–127.
[31] D. N. Srivastava, S. Chappel, O. Palchik, A. Zaban, A. Gedanken, *Langmuir* **2002**, *18*, 4160–4164.
[32] a) M. Wong, M. J. C. Hendrix, K. VonderMark, C. Little, R. Stern, *Dev. Biol.* **1984**, *104*, 28–36; b) M. T. Hincke, J. Gautron, M. Panheleux, J. Garcia-Ruiz, M. D. McKee, Y. Nys, *Matrix Biol.* **2000**, *19*, 443–453.
[33] a) K. Mann, J. Gautron, Y. Nys, M. D. McKee, T. Bajari, W. J. Schneider, M. T. Hincke, *Matrix Biol.* **2003**, *22*, 397–407; b) S. Poon, M. S. Rybchyn, S. B. Easterbrook-Smith, J. A. Carver, G. J. Pankhurst, M. R. Wilson, *J. Biol. Chem.* **2002**, *277*, 39532–39540.
[34] D. C. Pan, N. N. Zhao, Q. Wang, S. C. Jiang, X. L. Ji, L. J. An, *Adv. Mater.* **2005**, *17*, 1991–1995.
[35] J. M. Moss, M. P. I. VanDamme, W. H. Murphy, P. G. Stanton, P. Thomas, B. N. Preston, *Arch. Biochem. Biophys.* **1997**, *339*, 172–182.
[36] A. Dieguez, A. Romano-Rodriguez, J. R. Morante, J. Kappler, N. Barsan, W. Gopel, *Sens. Actuators B* **1999**, *60*, 125–137.
[37] a) D. F. Zhang, L. D. Sun, C. J. Jia, Z. G. Yan, L. P. You, C. H. Yan, *J. Am. Chem. Soc.* **2005**, *127*, 13492–13493; b) Y. Wang, J. Y. Lee, H. C. Zeng, *Chem. Mater.* **2005**, *17*, 3899–3903.

Received: December 12, 2006
Published Online: April 13, 2007

